RESEARCH ARTICLE

Editor's Choice

ADVANCED ELECTRONIC MATERIALS Open Access

www.advelectronicmat.de

Fully Transparent Epitaxial Oxide Thin-Film Transistor Fabricated at Back-End-of-Line Temperature by Suboxide Molecular-Beam Epitaxy

Felix V.E. Hensling, Patrick Vogt, Jisung Park, Shun-Li Shang, Huacheng Ye, Yu-Mi Wu, Kathleen Smith, Veronica Show, Kathy Azizie, Hanjong Paik, Debdeep Jena, Huili G. Xing, Y. Eren Suyolcu, Peter A. van Aken, Suman Datta, Zi-Kui Liu, and Darrell G. Schlom*

Transparent oxide thin film transistors (TFTs) are an important ingredient of transparent electronics. Their fabrication at the back-end-of-line (BEOL) opens the door to novel strategies to more closely integrate logic with memory for data-intensive computing architectures that overcome the scaling challenges of today's integrated circuits. A recently developed variant of molecular-beam epitaxy (MBE) called suboxide MBE (S-MBE) is demonstrated to be capable of growing epitaxial In_2O_3 at BEOL temperatures with unmatched crystal quality. The fullwidth at halfmaximum of the rocking curve is 0.015° and, thus, ≈5x narrower than any reports at any temperature to date and limited by the substrate quality. The key to achieving these results is the provision of an In_2O beam by S-MBE, which enables growth in adsorption control and is kinetically favorable. To benchmark this deposition method for TFTs, rudimentary devices were fabricated.

1. Introduction

The existence of transparent conductors has fueled the design and development of electronics for decades.[1] An application that is of central importance to the development of transparent electronics is transparent field-effect transistors. Thin-film transistors (TFTs) with oxides as active channel layers have proven especially promising in this regard. The prevalence of oxides as active layers is based on the one hand on the success of oxides in other transparent electronics applications e.g., photovoltaics and displays, and on the other hand on the prospect of added functionality.[2] A

F. V. Hensling, P. Vogt, J. Park, K. Azizie, H. Paik, D. Jena, H. G. Xing, Y. E. Suyolcu, D. G. Schlom
Department of Materials Science and Engineering
Cornell University
Ithaca, NY 14853, USA
E-mail: hensling@cornell.edu

P. Vogt
Institut für Festkörperphysik
Universität Bremen
28359 Bremen, Germany

S.-L. Shang, Z.-K. Liu
Department of Materials Science and Engineering
The Pennsylvania State University
University Park, PA 16802, USA

H. Ye, S. Datta
Department of Electrical Engineering
University of Notre Dame
Notre Dame, IN 46556, USA

Y.-M. Wu, Y. E. Suyolcu, P. A. van Aken
Max Planck Institute for Solid State Research
Heisenbergstraße 1, 70569 Stuttgart, Germany

K. Smith, D. Jena, H. G. Xing
School of Electrical and Computer Engineering
Cornell University
Ithaca, NY 14853, USA

V. Show, H. Paik
Platform for the Accelerated Realization
Analys, and Discovery of Interface Materials (PARADIM)
Cornell University
Ithaca, NY 14853, USA

H. Paik
School of Electrical and Computer Engineering
University of Oklahoma
Norman OK 73019, USA

D. G. Schlom
Kavli Institute at Cornell for Nanoscale Science
Ithaca, NY 14853, USA

D. G. Schlom
Leibniz-Institut für Kristallzüchtung
12849 Berlin, Germany

The ORCID identification number(s) for the author(s) of this article can be found under https://doi.org/10.1002/aelm.202400499

DOI: 10.1002/aelm.202400499

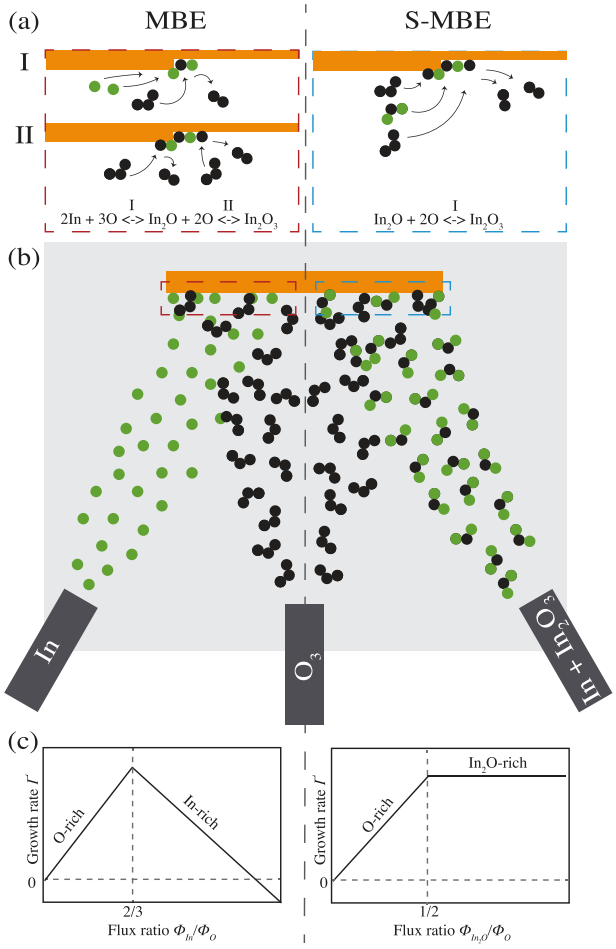

Figure 1. Schematic comparison of the growth of In_2O_3 by MBE (left) with S-MBE (right). Indium is represented by green circles and oxygen by black. a) Shows how S-MBE skips the first reaction step simplifying the formation of In_2O_3. This is enabled by the mixed In+In_2O_3 source supplying In_2O instead of In metal b). The active oxygen radical released by O_3 is the active oxidant. The volatility of In_2O allows an adsorption-controlled growth of In_2O_3 as long as enough In_2O is supplied as shown in c) and the substrate temperature is sufficiently high. For MBE an oversupply of indium results in the formation of volatile In_2O, but insufficient oxidant to further oxidize the In_2O to In_2O_3 during the residence time of the In_2O on the substrate surface. The result is a decrease in the growth rate of the In_2O_3 film as the flux of indium is increased.

variety of oxides has been probed as active channel layers for TFTs of which the most promising ones are based on indates[3–9] and stannates.[10] It is preferred to have the active layer of transistors in epitaxial form. This is because the defects that exist in polycrystalline and amorphous films, specifically grain boundaries or dangling bonds, can result in traps that degrade device performance.[2,10] A major drawback of epitaxial growth, however, is that it usually requires high temperatures.[11] This contradicts the industry's desire to fabricate TFTs at back-end-of-line (BEOL) temperatures which would ultimately enable a monolithic 3D (M3D) integration scheme in which logic is immersed in memory – an effective strategy to overcome today's scaling problems in memory technologies.[12,13] Up to now the strategy to fulfill the thermal budget for the active oxide layer has been to avoid epitaxial deposition. Impressive results have been reported for amorphous In_2O_3[4–9] and W-doped In_2O_2[3] films as active oxide layers deposited at BEOL temperatures. In this paper, we exploit a recently developed deposition technique, suboxide molecular beam epitaxy (S-MBE),[14,15] to grow epitaxial In_2O_3 layers at a temperature below 450 °C. In addition to satisfying the BEOL thermal budget, we are able to grow epitaxial In_2O_3 with unmatched structural perfection. Finally, we present device results demonstrating the promising performance of In_2O_3 TFTs fabricated on these epitaxial films.

We choose In_2O_3 as the epitaxial active oxide for two main reasons. First, recent results on amorphous In_2O_3 show its potential for superior BEOL TFTs[9] based on the high mobilities achieved.[16,17] Second, a relatively obscure[18–23] and underutilized variant of MBE was recently shown to provide major advantages for the growth of β-Ga_2O_3 films and dubbed S-MBE,[14,15,24,25] giving us reason to believe that it will also significantly improve the quality of In_2O_3 films. Here, we will for the first time explain the application of S-MBE to the epitaxial growth of In_2O_3, and why it results in superior crystal quality even at BEOL temperatures.

Despite being a mere binary compound, the growth of In_2O_3 is challenging. Even the best films in the literature usually show a wide variety of multidimensional defects including faceting, tilt relaxation, antiphase boundaries, and dislocations. This is especially true for the energetically less favorable (001)-oriented surface, commonly achieved by growing on (001)-oriented yttria-stabilized zirconia (YSZ) substrates. [26–28] These YSZ substrate contain 9.5 mol% Y_2O_3, which is sufficient to make YSZ cubic. The (001) orientation of In_2O_3 is also the preferred growth orientation for electronic applications as films with this orientation generally show higher electron mobilities.[17,29,30] While the relatively high lattice mismatch between In_2O_3, which has the bixbyite structure, and YSZ (1.9%) and the lack of bixbyite commercial substrates surely play a role in the wide variety of defects in In_2O_3 (001)-oriented films, here we show that growth by S-MBE on well-oriented YSZ (001) substrates can improve the achievable crystal quality immensely. We found that only substrates with a miscut of less than 0.1° (Crystec GmbH) resulted in the reported high film quality.

2. S-MBE of In_2O_3 at BEOL Temperature

2.1. Growth and Surface Characterization

For conventional MBE the formation of In_2O_3 at the substrate surface can be described by the following two-step reaction, where the first step is the rate-limiting step:[14,31–33]

$$2\,In + 3\,O \leftrightarrow In_2O + 2\,O \leftrightarrow In_2O_3 \quad (1)$$

This reaction is schematically depicted in the top left of **Figure 1**. It is the first step that defines the narrow growth window of today's most perfect epitaxial In_2O_3 films. For conventional MBE processes the achievable growth rate and perfection are defined by the applicable oxidant pressure (p_{O_3}). When the indium flux exceeds the available oxygen flux needed to complete both of the reaction steps in Equation (1), the growth rate of In_2O_3

will decrease (Figure 1c). This is due to the volatility of the intermediate product, the suboxide In_2O. Indium species in surplus of the supplied oxygen provided by the oxidant, will either only form the volatile In_2O that desorbs before it is oxidized further to In_2O_3, or in the most extreme case react with already formed In_2O_3 to form In_2O, which corresponds to etching (see Equation (1)).[14,31–33] The aim of S-MBE is to circumvent the first rate limiting step of the two-step reaction in order to achieve higher growth rates and potentially higher quality films.[30] A route to achieve this is to provide a molecular beam of In_2O directly to the substrate in place of the molecular beam of indium used in conventional MBE (Figure 1b). An additional advantage of employing In_2O as a molecular beam is that its volatility enables adsorption-controlled growth, the key to growing high-quality films generally by MBE.[15,34–40] The most straightforward way to obtain an In_2O beam is to use an In_2O_3 source, which thermodynamic calculations have shown to result in an In_2O molecular beam.[41] Unfortunately, it also requires inconveniently high temperatures for a transition into the gas phase, ultimately decreasing achievable purities. Although, pure oxide sources have been used to bypass the rate-limiting step for similar material systems,[42,43] the resulting films have been limited by undesired impurities coming from the crucibles at the high temperatures required for evaporation,[44,45] low growth rates,[46] or unstable sources.[47]

We circumvent these issues by supplying the suboxide beam, in this case In_2O, from a mixture of In_2O_3 and elemental indium. To identify the ideal composition, **Figure 2a** shows the In-O phase diagram predicted using the Scientific Group Thermodata Europe (SGTE) Substance Database (SSUB5)[48] within the Thermo-Calc software.[49] The region of interest is between 0 and 60 mol% O where between 420 and 920 K a two-phase region of In_2O_3 (s) and In (ℓ) is found. It is important to note that within this region mixtures containing 33 mol% O must be avoided, as with an increasing temperature this mix passes through the heteroazeotrope – resulting in a spontaneous transition of all condensed phases into the gas phase. We, thus consider mixtures to the left and the right of the heteroazeotrope, i.e., 20 mol% O and 40 mol% O. Above 920 K for 20 mol% O the mix transitions into a two-phase region of gas and In (ℓ), and for 40 mol% O into a two-phase region of gas and In_2O_3 (s), respectively. The mix of 20 mol% O transitions into the gas phase at 1075 K and the mix of 40 mol% O at 1400 K. This already shows the benefit of the 40 mol% O mixture as it is usable over a wider temperature range. The benefit of a 40 mol% O mixture is further established by comparing the partial pressure ratio between In_2O and indium in the gas phase for both mixtures in Figure 2b. Considering the dashed line which represents the 40 mol% O mixture and the solid line which represents the 20 mol% O mixture, it is evident that in the relevant region (920-1075 K for the 20 mol% O mixture and 920–1400 K for the 40 mol% O mixture) the gas phase of the 40 mol% O mixture provides a higher In_2O to indium ratio. The higher oxygen activity of the 40 mol% O mixture is also an advantage of the 40 mol% O mixture (Figure 2c). For all of these reasons, the 40 mol% O mixture is the preferable source for a molecular beam of In_2O for use in S-MBE.

As In_2O is a volatile species and, thus, enables the growth in an adsorption-controlled regime we, in principle, expect to reach

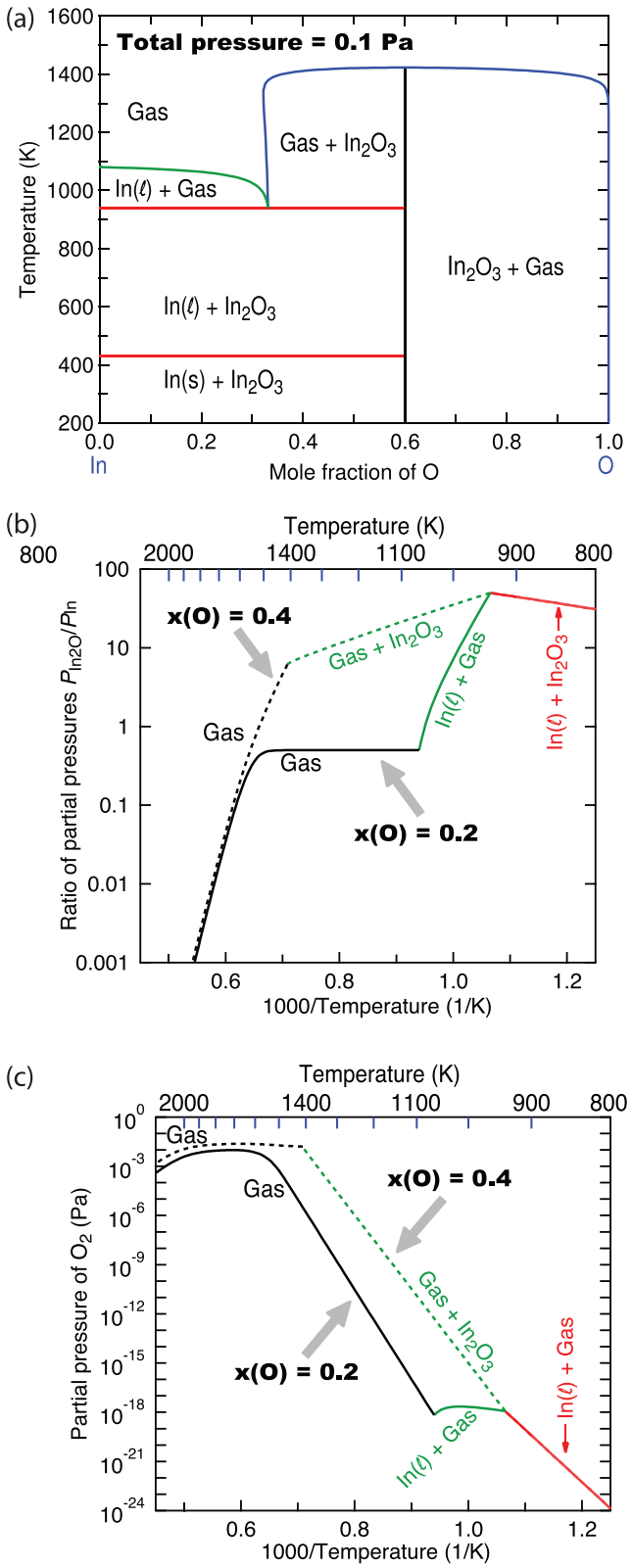

Figure 2. a) In-O temperature-composition phase diagram at a total fixed pressure of 0.1 Pa. b) Ratio of partial pressures of In_2O (P_{In_2O}) to that of In (P_{In}) and (c) O_2 partial pressure as a function of temperature for mixes with 0.2 mol% O (solid line) and 0.4 mol% O (dashed line), respectively. To skip the first step of Equation (1) a high ratio of P_{In_2O} is desired.

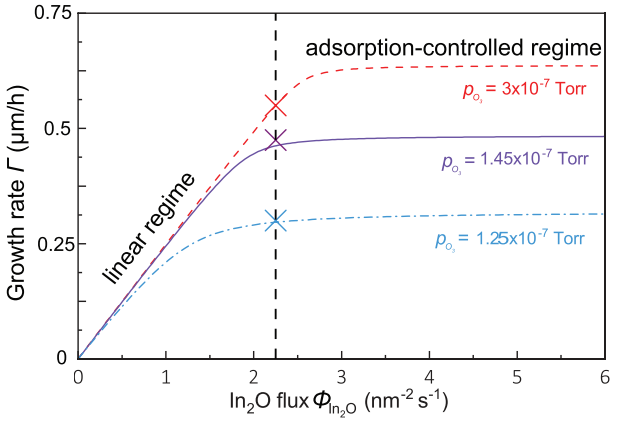

Figure 3. Relation between the flux of In_2O (Φ) in the molecular beam and the growth rate (Γ) of the In_2O_3 film. The vertical dashed line marks the applied In_2O flux in this work. The growth rate dependence of the flux for the three different applied oxidant pressures is fitted by the model described by Vogt et al.,[24] The crosses in the respective colors mark the growth regime resulting from the combination of the applied In_2O flux and oxidant pressure.

the ideal growth conditions as long as sufficient In_2O flux (Φ_{In_2O}) is supplied. Equivalently, when supplying a constant In_2O flux Φ_{In_2O} = 2.25 In_2O molecules nm^{-2}s and systematically decreasing the oxidant pressure, we expect to find a maximum oxidant pressure below which we are in an adsorption-controlled regime. The growth rate resulting from different applied In_2O fluxes at different oxidant pressures is visualized in **Figure 3**; the high growth rates, which can be increased further at higher oxidant pressures, are noteworthy.

A first assessment of the growth regime can be drawn from monitoring the real-time reflection high-energy electron diffraction (RHEED) pattern along the [110] azimuth of film and substrate. We expect 10 and $\bar{1}0$ streaks of epitaxial In_2O_3 films to appear at the half-order position of the respective streaks of the (001)-oriented YSZ substrate. This is because the lattice parameter of the fluorite YSZ is roughly half that of the bixbyite In_2O_3. **Figure** 4a–c shows the dependence of the RHEED pattern at the end of film growth on the applied oxidant pressure. For the highest oxidant pressure $p_{O_3} = 3 \times 10^{-7}$ Torr (Figure 4a) spots along the expected streaks are prominently visible indicating island formation. Nevertheless, the first-order Laue zone is visible at the edge of the field of view. Growth at a slightly lower background oxidant pressure, $p_{O_3} = 1.45 \times 10^{-7}$ Torr, results in a RHEED pattern (Figure 4b) with defined streaks, a first-order Laue zone, and Kikuchi lines, all indicative of a surface with high crystalline quality. Growth at a slightly lower oxidant pressure $p_{O_3} = 1.25 \times 10^{-7}$ Torr changes the appearance of the RHEED pattern (Figure 4c) yet again. While streaks are still clearly visible, the overall pattern gets hazy indicating amorphous content; also spots are visible again indicating the formation of islands. Nevertheless, the first-order Laue zone is still visible. The improvement of the crystalline quality derived from the RHEED patterns with the initial decrease of oxidant pressure is what we expect as explained above. It marks the transition into the adsorption-controlled regime. It is surprising, however, that the crystal quality seems to decrease again when further decreasing the oxidant pressure. To understand this, we first consider the associated surface morphologies.

Figure 4d–f shows the respective 5 × 5 µm^2 surface morphologies. The surface of the sample grown under the highest oxidant pressure has, as expected from the corresponding RHEED pattern, a relatively rough surface with an rms of 1.91 nm. The surface of the intermediate pressure $p_{O_3} = 1.45 \times 10^{-7}$ Torr sample Figure 4e has, in agreement with the RHEED pattern, an outstandingly smooth surface with an rms of 0.45 nm. The surface morphology of the sample grown with a slightly lower oxidant pressure $p_{O_3} = 1.25 \times 10^{-7}$ Torr confirms that something unexpectedly changes upon a decrease in the process pressure. Islands of significant height are visible and, thus, the rms is very high (15.9 nm).

While RHEED and AFM are both surface-sensitive techniques, X-ray diffraction (XRD) allows an investigation of the underlying crystal quality. With its sensitivity to the crystalline perfection of the entire film, we give foremost consideration to the $\theta - 2\theta$ diffractograms and the rocking curves of the films shown in **Figure** 5a,b. Figure 5a shows the $\theta - 2\theta$ scan of all three films in the vicinity of the YSZ 001 peak between a 2θ of 34° and 37°. Two remarkable features strike the eye. First, except for the film grown at $p_{O_3} = 3 \times 10^{-7}$ Torr the 3_s-2_f hybrid peak is visible in the spectra. Hybrid peaks are only observed for extremely high film qualities.[50] Its occurrence confirms the high quality of the film grown at $p_{O_3} = 1.45 \times 10^{-7}$ Torr indicated by RHEED and AFM. It is surprising that we also observe the hybrid peak for $p_{O_3} = 1.25 \times 10^{-7}$ Torr where RHEED and AFM indicated non-ideal growth conditions. The second remarkable feature is that we can observe thickness fringes for the film grown at $p_{O_3} = 1.45 \times 10^{-7}$ Torr despite the high thickness (150 nm) and those not being observed for In_2O_3 (001)-oriented films previously. This once more emphasizes the high crystal and surface quality of the film.

The excellent structural perfection is also confirmed by the rocking curves in Figure 5b. The rocking curve of the $p_{O_3} = 3 \times 10^{-7}$ sample has a FWHM of 0.06° and as can be seen from **Table** 1 is still better than any literature report. The film grown at $p_{O_3} = 1.45 \times 10^{-7}$ Torr has a rocking curve with a FWHM of only 0.015°, which is more than 5x narrower than any film in Table 1, and has reached the limitation set by the quality of the underlying substrate (black rocking curve in Figure 5b). The high FWHM value of the film grown at $p_{O_3} = 1.25 \times 10^{-7}$ Torr is unexpected considering the occurrence of the hybrid peak in the very same film. Table 1 lists representative examples for of the FWHMs of rocking curves of In_2O_3 grown on (001)-oriented YSZ by different methods. It is striking that independent of the growth method the achievable FWHM, even at significantly higher substrate temperatures (T_{sub}), is relatively high and never close to the substrate quality. Our film grown by S-MBE at the ideal oxidant pressure stands out markedly in this comparison with the best reported films.

The excellent structural perfection of the film grown under ideal conditions, including sharp interfaces, is corroborated by STEM. **Figure** 6a shows a low-magnification cross-sectional STEM image of the same optimal sample. The uniform microstructure of the film and sharp interfaces are evident. The blue rectangle marks the zoomed-in region represented in Figure 6b. As expected from the rocking curve, no extended defects are

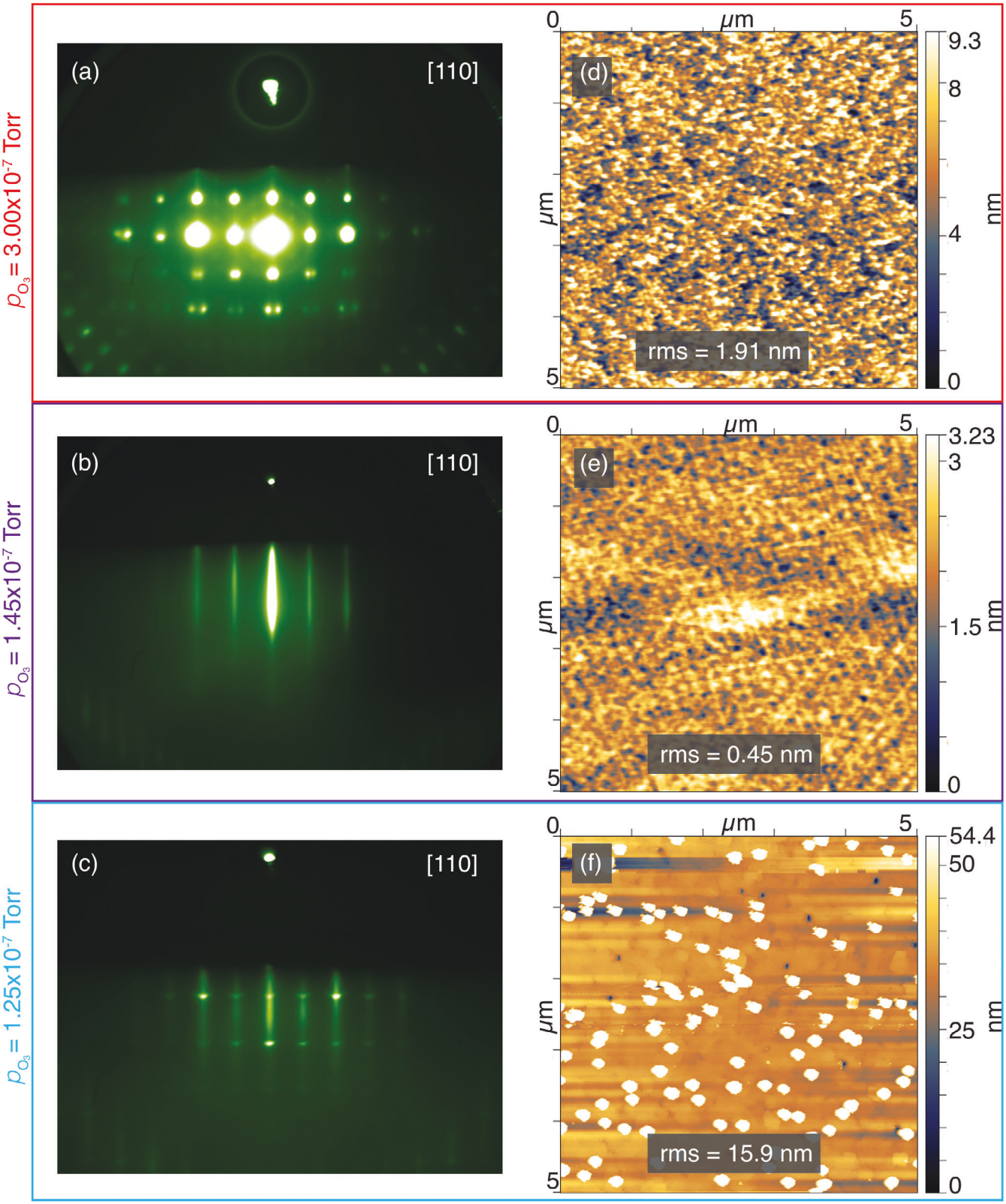

Figure 4. a–c) Representative RHEED patterns with the electron beam incident along the [110] azimuth captured at the end of the deposition. d–f) Surface morphologies of the ≈150 nm thick films including the rms roughness. The different RHEED patterns and surface morphologies are a direct result of the different applied oxidant pressures that are indicated on the left.

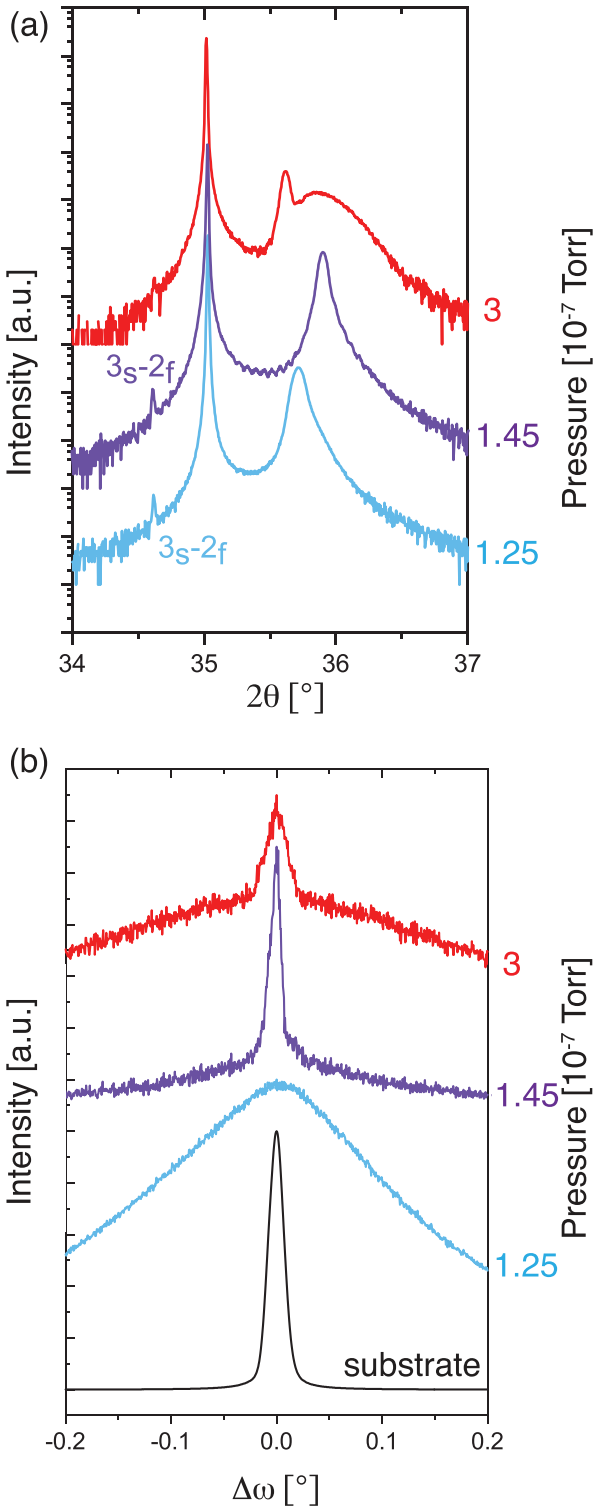

Figure 5. a) $\theta - 2\theta$ X-ray diffraction scan of ≈150 nm thick In_2O_3 films grown at different background oxidant pressures indicated on the vertical axis on the right. The 3_s-2_f hybrid peak is observed for the films grown at lower pressures, where the subscript *s* refers to the substrate (the 003 substrate peak) and the subscript *f* refers to the film peak (the 002 film peak). b) Rocking curves of the 004 peak of the same films, together with a rocking curve of a representative (001)-oriented YSZ substrate for comparison, all shifted along the vertical axis for clarity.

Table 1. FWHM of the rocking curves in Figure 5b in comparison with literature[26,29,106,107] sorted by growth temperature.

Growth Temperature [°C]	Growth Method	FWHM [°]	Refs.
300	MBE	0.08	[106]
< 450	S-MBE	0.060	this work ($p_{O_3} = 3 \times 10^{-7}$)
< 450	S-MBE	0.015	this work ($p_{O_3} = 1.45 \times 10^{-7}$)
< 450	S-MBE	0.271	this work ($p_{O_3} = 1.25 \times 10^{-7}$)
550	RF-sputtered	0.54	[107]
650	MBE	0.11	[26]
950	CVD	0.083	[29]

visible. The nominally featureless microstructure observed is in stark contrast to prior STEM studies of In_2O_3 films grown on YSZ (001), where a wide array of extended defects was unraveled.[27,28] Figure 6c represents the area marked by an red box in Figure 6b. The interface is atomically sharp.

The strong dependence of the microstructure of the In_2O_3 films on the oxygen pressure in which they are grown by S-MBE can be understood with the help of the plot shown in Figure 3. Here, the dependence of the film growth rate on the In_2O flux is shown. The growth rate was fitted by our recently developed model[24] for the respective pressures $p_{O_3} = 1.45 \times 10^{-7}$ Torr (blue dashed), $p_{O_3} = 1.25 \times 10^{-7}$ Torr (purple solid), and $p_{O_3} = 3 \times 10^{-7}$ Torr (red dashed). The validity of the fit was verified by X-ray reflectivity measurements. The applied In_2O flux of $\Phi_{In_2O} = 2.25$ In_2O molecules $nm^{-2}s$ is marked by the black dashed line. S-MBE aims for a growth regime to the right of the transition region (the region with the highest curvature) between the linear regime and the adsorption-controlled regime. It is thus trivial to understand why an increased oxidant pressure results in worse films. The high pressure leads to leaving the adsorption-controlled plateau and moving into the oxygen-rich linear regime. It is less straightforward, however, to understand why a decrease in the oxidant pressure results in decreased film quality. In theory, we only expect a lower growth rate as the In_2O for which there is now insufficient oxidant to complete Equation (1) should desorb. But does all of the excess In_2O actually desorb at the low growth temperatures we have utilized in this study in order to fulfill the BEOL requirements? Our hypothesis is no. At the < 450 °C substrate temperature of this study, the excess In_2O does not desorb but rather sticks to the surface. At higher T_{sub} the excess In_2O can fully desorb. When the film grown at $T_{sub} < 450$ °C is later cooled down and exposed to air, the adsorbed In_2O on the film surface oxidizes and forms epitaxial In_2O_3 islands as can be seen in the topography (Figure 4f). The resulting In_2O_3 islands are, however, not formed with the same uniformity and high surface diffusion as the underlying epitaxial film. It is this underlying layer that is responsible for the hybrid diffraction peak observed in XRD. In contrast, the not desorbed In_2O excess on the film surface that oxidizes at a later point is responsible for the rough surface and the broadened rocking curve.

The characterization of the epitaxial In_2O_3 grown at below BEOL temperatures shows that S-MBE indeed enables to skip the first limiting reaction step (Equation (1)). This in turn lifts kinetic limitations on the crystalline In_2O_3 formation and the growth in a

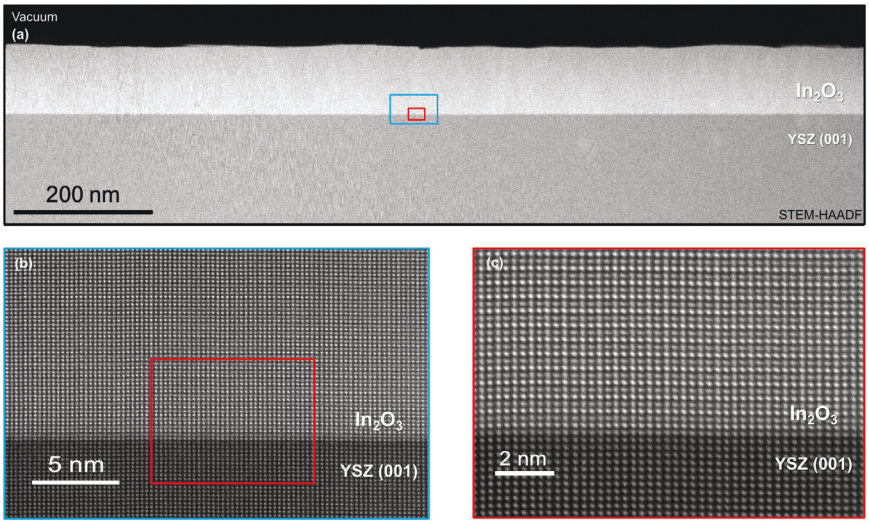

Figure 6. a) Low-magnification STEM-HAADF overview image showing the uniformity of the surface, interface, and the film grown on YSZ (001) at an oxidant pressure of 1.45×10^{-7} Torr. b) High magnification of the area highlighted by the blue rectangle in (a). c) Zoom into the interface region marked in red revealing the well-ordered structure allowing the sharpness of the interface to be discerned with atomic resolution.

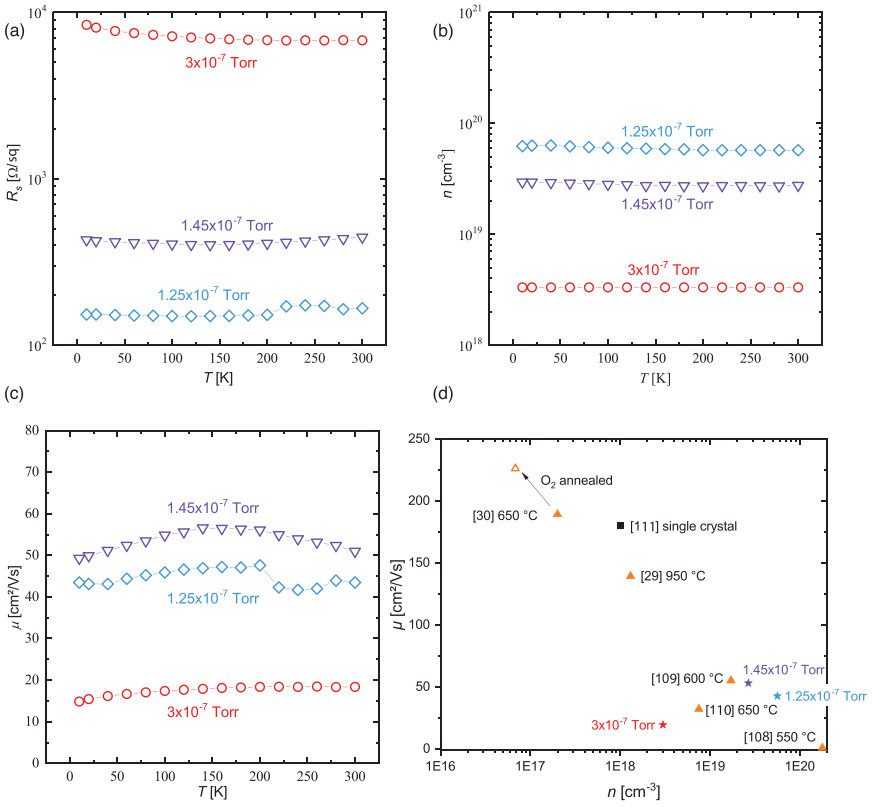

Figure 7. a–c) Temperature-dependent electrical measurements of (a) sheet resistance, (b) carrier concentration, and (c) mobility of the ≈ 150 nm thick In_2O_3 films grown at the oxidant pressures 1.25×10^{-7} Torr (blue), 1.45×10^{-7} Torr (purple), and 3×10^{-7} Torr (red). d) Comparison of the dependence of the room-temperature mobility on the carrier concentration of the films in this study with a single crystal and other epitaxial In_2O_3 films from the literature.[29,30,107–110] The growth temperature is indicated for the films from the literature. Our samples are grown at below 450 °C at the indicated oxidant pressures.

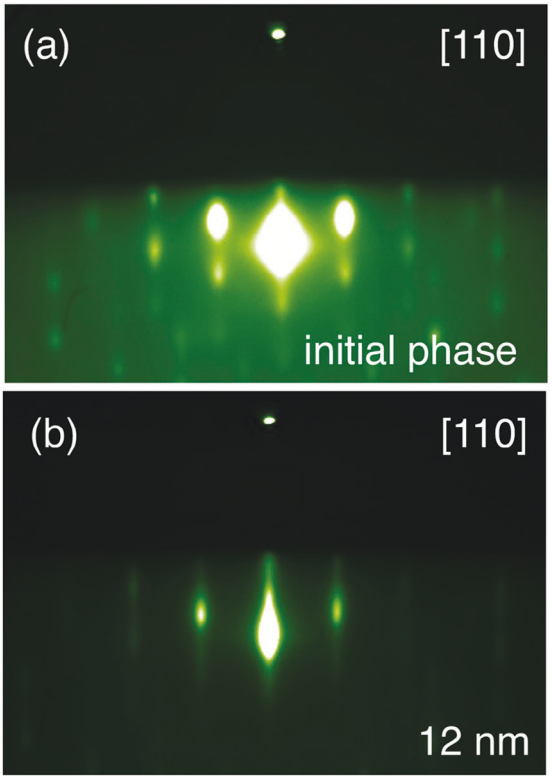

Figure 8. RHEED pattern of an In_2O_3 film grown at 1.45×10^{-7} Torr captured a) after a few seconds and b) after the initial 12 nm of growth. The film transitions slowly into the ideal growth regime as the local activity of oxygen is higher upon the bare substrate than it is in the steady state after several nm of In_2O_3 has been deposited.

quasi-adsorption controlled regime resulting in unmatched crystal qualities of the films.

2.2. Electrical Properties

Having discovered how to achieve unmatched structural perfection even at BEOL temperatures, the next step is to investigate the electrical properties of these optimized films. **Figure 7a** shows the sheet resistance of the In_2O_3 films grown at $p_{O_3} = 1.25 \times 10^{-7}$ Torrr (blue), $p_{O_3} = 1.45 \times 10^{-7}$ Torr (purple), and $p_{O_3} = 3 \times 10^{-7}$ Torr (red). The sheet resistance is seen to be low and largely independent of temperature for the films grown at $p_{O_3} = 1.25 \times 10^{-7}$ Torr (174 Ω sq^{-1}) and $p_{O_3} = 1.45 \times 10^{-7}$ Torr (331 Ω sq^{-1}), as is typical for a degenerate semiconductor. The slight upturn in the sheet resistance at low temperature of the sample grown at $p_{O_3} = 3 \times 10^{-7}$ Torr indicates localization. The carrier concentrations extracted from Hall effect measurements on these samples are shown in Figure 7b. Hall indicates that the charge carriers are electrons and that the electron concentration is constant over the whole temperature range and scales with the oxidant pressure. This indicates that the carriers in these nominally undoped films arise from doping by oxygen vacancies, i.e., In_2O_{3-x}. Figure 7c shows the temperature-dependence of the electron mobility. Counter-intuitively, the two samples with the highest carrier concentrations, $p_{O_3} = 1.25 \times 10^{-7}$ Torr (42.4 cm^2 Vs^{-1}) and $p_{O_3} = 1.45 \times 10^{-7}$ Torr (52.9 cm^2 Vs^{-1}), also exhibit the highest electron mobility while the sample with the lowest carrier concentration, grown at $p_{O_3} = 3 \times 10^{-7}$ Torr, has a markedly lower mobility (19.1 cm^2 Vs^{-1}).

This can be understood if we consider the structural data discussed above. The sample grown at $p_{O_3} = 3 \times 10^{-7}$ Torr was not grown in the adsorption-controlled regime, to the right of the kink in Figure 3. This results in a lower crystallinity and, thus, more scattering, in turn resulting in the lower mobility and

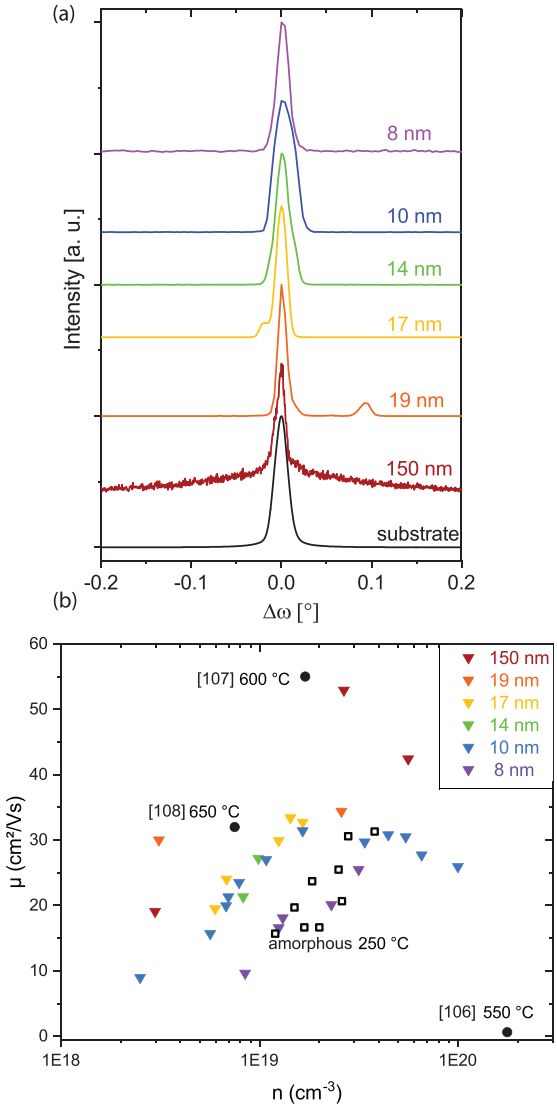

Figure 9. a) Rocking curves of samples as a function of film thickness (offset for clarity) in comparison to the substrate rocking curve (black). For all samples the FWHM is dominated by the substrate quality. Samples thinner than 150 nm are grown with dynamic adjustment of the oxidant pressure. b) Comparison of the dependence of the room-temperature mobility on the carrier concentration of our films grown by S-MBE and films from literature (black dots).[107–109] The growth temperature is indicated for the film results taken from the literature. Our samples are grown at below 450 °C. The thickness of our In_2O_3 films grown by S-MBE is represented by the same colors as in (a). An additional comparison is drawn to amorphous tungsten doped In_2O_3 films (black open squares).

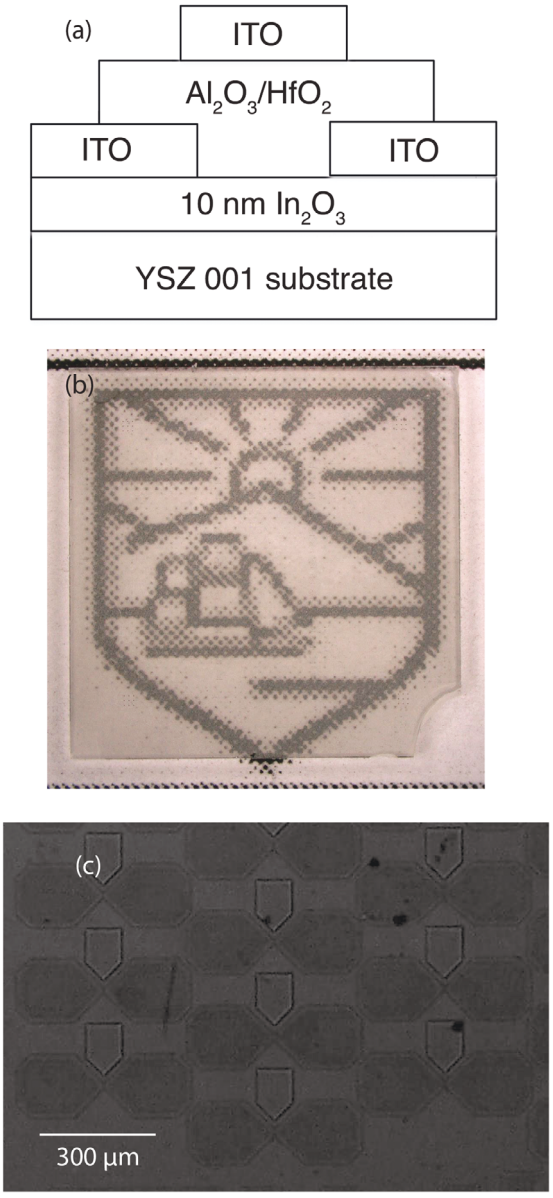

Figure 10. a) Schematic of the cross-section of the thin-film transistor structure. b) Brightfield micrograph of an epitaxial In_2O_3 10 × 10 cm^2 sample grown by S-MBE with a transistor structure as shown in (a) demonstrating the full transparency of the devices. c) Darkfield micrograph of the same sample at a higher magnification where the outline of the transistor structures can be seen.

localization at low temperatures. For the samples grown at $p_{O_3} = 1.25 \times 10^{-7}$ Torr and $p_{O_3} = 1.45 \times 10^{-7}$ Torr the mobility scales with the carrier concentration. This is due to the high crystal quality of the bulk of both films. As explained above, the sample grown at $p_{O_3} = 1.25 \times 10^{-7}$ Torr has – despite the imperfect surface – an underlying epitaxial film with high structural quality which dominates its conductivity. The structure of the respective films is, thus, the dominant variable influencing the resulting conductivity.

In comparison to existing literature, the mobility of our samples is on par with other samples with comparably high carrier concentrations as illustrated in Figure 7d. Nonetheless, we achieve these mobilities at significantly lower growth temperatures. We ascribe this to the higher structural perfection of the films grown under optimal conditions by S-MBE. We find it noteworthy that in the same work in which Bierwagen et al., used conventional MBE to grow In_2O_3 films with the highest mobilities ever reported, they also report only being able to achieve mobilities of 5.5 cm^2 Vs^{-1} at a growth temperature of 550 °C.[30] This shows the significant difference in surface kinetics for the growth of In_2O_3 films by conventional MBE versus S-MBE.

3. BEOL-Compatible Epitaxial In_2O_3 TFTs

3.1. Growth of the Oxide Channel Material

As we can grow In_2O_3 films of unmatched structural perfection at BEOL temperatures with high mobilities, the consequent next step is to apply these films to actual devices. To make TFTs with high on/off ratios, it is important to be able to fully deplete the In_2O_3 channel. This means having good control of the carrier concentration of the conductive In_2O_{3-x} films. Unfortunately, a central challenge in the preparation of In_2O_3-based devices is controlling the carrier concentration.[5] This difficulty is linked to the energetic preference of In_2O_3 to exhibit unintentional doping.[17] Si et al., proposed that the electron concentration of amorphous In_2O_3 films can be controlled by simply reducing the film thickness.[5] For epitaxial In_2O_3, the challenge with this approach is the degraded structural and electrical properties of the initial epitaxial In_2O_3 grown upon the YSZ (001) substrate. **Figure 8**a shows the RHEED pattern of the film grown at $p_{O_3} = 1.45 \times 10^{-7}$ Torr, which ultimately results in the pattern of Figure 8b. It strikes the eye that the initial phase of growth does not exhibit the expected streaky pattern as seen in Figure 8b. We attribute this to the high oxygen ion conductivity of YSZ,[51] which increases the oxygen activity above that provided by the oxygen partial pressure alone. To counter this interfacial effect, a lower oxygen partial pressure can be provided during the growth of thinner films to remain at the knee of the curve shown in Figure 3. Unfortunately, the window of applicable oxidant pressures is small as discussed in the previous section.

The rocking curves in **Figure 9**a show that we can maintain the superior crystal quality down to an In_2O_3 film thickness of 8 nm by applying lower oxidant pressures for the initial phase of the growth. Figure 9b shows the dependence of the film mobility on the carrier concentration for films with the same thickness. It zooms into the relevant part of Figure 7d with the literature references now marked by black solid dots and the thick films now marked by red triangles. As an additional reference, the µ(n) data for amorphous tungsten-doped In_2O_3 films are also shown (details on their fabrication are found in the experimental section). This is especially relevant as these amorphous tungsten doped In_2O_3 layers represent the oxide channel material of the benchmark devices shown in Figure 12.[3]

Figure 9 reveals that although epitaxial In_2O_3 films can be grown with thicknesses down to 8 nm, the mobility of thinner

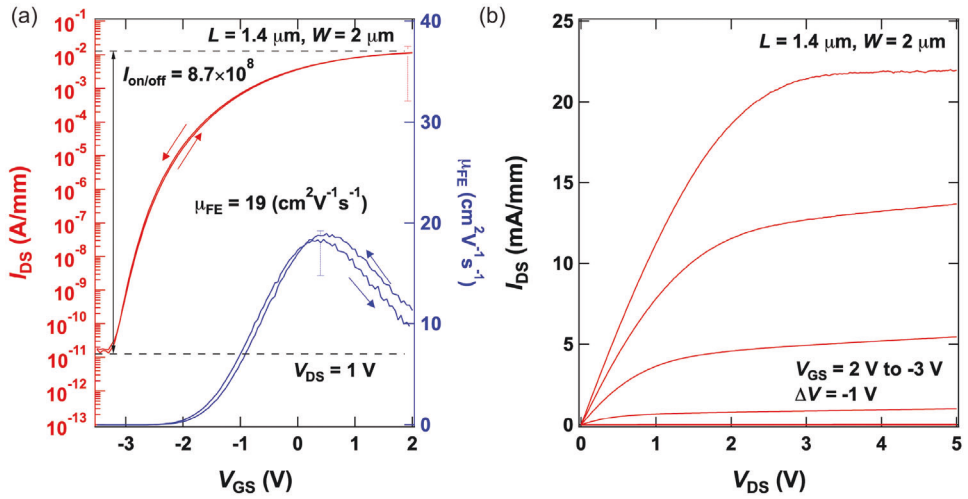

Figure 11. a) Transfer characteristics and mobility of a device with Al_2O_3 as an insulator with the variability marked by the vertical dashed lines. b) Output characteristics of the same device.

films is notably lower. This decrease becomes increasingly significant the thinner the film gets. The decreased film mobility is likely a result of an increasing influence of scattering at the imperfect interface. A mobility dome is revealed which for all thicknesses is in the low 10^{19} cm^{-3} carrier concentration regime. Choosing the ideal films for device fabrication, thus, comes along with compromising between the highest possible mobility and the ability to deplete the carriers in the channel for the TFT. Comparing our films with the benchmark amorphous films, however, it is obvious that we can achieve better or at least equally good mobility carrier concentration combinations. This motivates the fabrication of TFTs from these films as described in the next section.

3.2. Device Performance

Considering Figure 9b we decided on 10 nm of oxide channel material as it is the lowest film thickness where the mobility does not decrease as markedly as for 8 nm. A schematic of the devices fabricated is shown in **Figure 10a**; full details are provided in the experimental section. As is evident from the dimensions and design these are rudimentary devices aiming to provide a proof of concept. Figure 10b shows a bright-field micrograph of a 10 × 10 mm^2 sample fabricated into transistors. As all of the constituent materials of the transistor layout are transparent in the visible spectrum, the resulting devices are also fully transparent. In the dark-field micrograph at a higher magnification

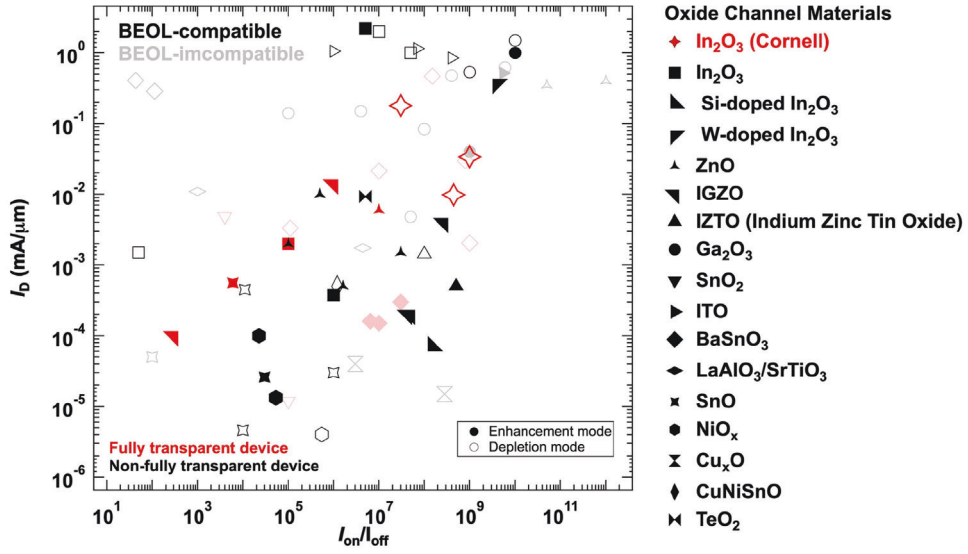

Figure 12. Comparison of the achievable saturation drain current I_D and on/off ratio of the current I_{on}/I_{off} achieved for the devices shown in this work (red stars) together with benchmark values from the literature.[3,53–103] Devices fabricated at BEOL-incompatible temperatures are shaded. Fully-transparent devices are marked in red. Not fully transparent devices usually rely on a non-transparent contact. Devices operated in enhancement mode are marked solid and devices operated in depletion mode are marked with open symbols.

in Figure 10c, features of the actual transistors can be discerned.

Figure 11 shows the device characteristics of a device with 10 nm In_2O_3 channel layer and Al_2O_3 as gate dielectric. The transfer characteristics are reproducible on the same sample as shown by the dashed error bars. Identical devices with a HfO_2 gate dielectric were fabricated and their device characteristics are shown in supporting information Figure S1 (Supporting Information). While the achievable drain saturation current for these devices is between one and two orders of magnitudes higher, they have a lower achievable mobility. The TFTs with a HfO_2 gate dielectric suffer from two additional drawbacks: 1) a significant variability in the device performance and 2) a counterclockwise hysteresis. (1) is likely the result of a small misalignment e.g., when part of the channel layer is not covered by the top gate electrode, the drain current will increase while the on/off ratio will decrease. Likely the TFTs with an Al_2O_3 gate dielectric were better aligned. The counterclockwise hysteresis of the HfO_2 gate insulator devices cannot be a result of ferroelectric HfO_2 as the material is amorphous. A likely explanation is the formation of dipoles at the HfO_2 interfaces as observed by Miyata.[52] Again, this drawback is not observed for the Al_2O_3 gate dielectric TFTs. Thus, despite the inferior drain saturation current, Al_2O_3 in our case is the preferable gate dielectric.

In addition to demonstrating proof-of-concept devices, comparing their performance with current state-of-the-art TFTs made from a variety of oxide semiconductors reveals their potential. **Figure 12** compares the performance of the device shown in Figure 11 and Figure S1 (Supporting Information) (marked by red stars) with current state-of-the-art devices which are sorted by six categories.[3,53–103] The shaded symbols indicate devices grown at BEOL incompatible temperatures and, thus, do not really compete. Open symbols denote depletion-mode TFTs and full symbols denote enhancement-mode TFTs. While enhancement-mode is generally preferable, given the high conductivity of our films it is unlikely to be achieved for epitaxial In_2O_3 devices. Devices marked in red are fully transparent while devices marked in black contain a non-transparent material - usually the metal contacts. If we only consider fully transparent BEOL devices, the devices shown in this work actually outperform all others. Nonetheless, it is not a big technological hurdle to make transparent metal contacts so ultimately it must be the aim to outperform the devices marked in black as well. With the exception of two data point based on Ga_2O_3 which were achieved on cleaved and transferred flakes - a technology that is not scalable - all devices outperforming our devices are based on amorphous In_2O_3-based materials.

If we consider the electrical properties of our films in comparison with the amorphous In_2O_3 films shown in Figure 9b it is likely that ultimately the epitaxial films grown as presented in this work can outperform their amorphous counterparts. The obvious route is downscaling the devices. For this proof-of-principal study we utilized simple optical lithography, resulting in a channel length of $L = 1.4\,\mu m$. In comparison, the devices currently outperforming ours have channel lengths between 40 and 200 nm. Equation (2) gives the dependence of the saturation drain current, I_D, on the channel length width (W), mobility (μ), gate oxide capacitance (C_{Ox}), gate to source voltage (V_{GS}), and threshold voltage (V_T).[104] From this equation it is clear that a more aggressive scaling of our devices should drastically increase the achievable drain current.

$$I_D = \frac{W\mu C_{Ox}}{2L}(V_{GS} - V_T)^2 \quad (2)$$

4. Conclusion

We unraveled the details and benefits of epitaxial In_2O_3 growth by S-MBE. We utilized these advantages to grow In_2O_3 at BEOL temperatures with superior structural perfection as evidenced by rocking curves, hybrid peaks and thickness oscillation in diffractograms, and STEM. We integrated these epitaxial films grown at below 450 °C into simple yet fully transparent transistor structures. Our results demonstrate the tremendous potential of In_2O_3 grown by S-MBE for TFTs.

5. Experimental Section

Characterization and Growth: All epitaxial In_2O_3 films were grown in a Veeco Gen10 MBE with a SUMO medium-temperature MBE effusion cell (Sumo is a registered trademark of Veeco Instruments, Inc.). Distilled ozone[105] was used as an oxidant. The samples were cooled in the same oxidant pressure in which they were grown to avoid the formation of additional oxygen vacancies. The substrate temperature was monitored by a thermal couple in between the heating element and the substrate. The thermocouple overestimates the temperature and it was ensured not to exceed 450 °C. The flux of the In_2O molecular beam is measured by a quartz-crystal microbalance (QCM). The 10 nm amorphous tungsten-doped In_2O_3 films were sputtered at room temperature with argon as a working gas. They were subsequently annealed in different O_2 atmospheres at 250 °C to alter the carrier concentrations. Film thickness is measured by X-ray reflectivity (XRR) obtained with a Panalytical Empyrean with Cu-Kα1 radiation as are the X-ray diffraction scans. The surface morphology was measured by using an Asylum Research Cypher ES atomic force microscope (AFM). Electrical transport measurements were performed in a 4-point van-der-Pauw geometry with a Quantum Design 9T PPMS. The TEM specimen preparation consisted of three main steps: i) mechanical grinding (down to 0.1 mm), ii) tripod wedge polishing (with an angle of 1.5°), and iii) double-sided argon-ion milling. For argon-ion thinning, a precision ion polishing system II (PIPS, Model 695) was used at low temperature. Immediately before the experiment, samples were treated in a Fischione plasma cleaner in a 75% argon–25% oxygen mixture. For STEM analyses, a probe-aberration-corrected JEOL JEM-ARM200F STEM equipped with a cold field-emission electron source and a probe Cs-corrector (DCOR, CEOS GmbH) was operated at 200 kV. STEM-HAADF imaging was performed at probe semi-convergence angle of 20 mrad that results in probe size of 0.08 nm and the collection angle range for HAADF imaging was 110–270 mrad.

Device Fabrication: To avoid the formation of undesired additional oxygen vacancies during etching a fabrication process originally developed for $BaSnO_3$ based TFTs was employed.[10] Device patterning and fabrication was, except for the atomic layer deposition of HfO_2, performed at Cornell's NanoScale Science and Technology Facility (CNF). The channel layer was etched by reactive ion etching with a mix of chlorine and argon gas in a PT720/740 RIE tool and photolithography was achieved using an Autostep 200. For device isolation the etching depth of the channel layer was chosen to be significantly deeper than the channel layer thickness. Tin-doped In_2O_3 was deposited as source and drain contact material by a PVD75 sputtering tool and patterned by lift-off. The 20 nm blanket HfO_2 and Al_2O_3 layers were deposited over the whole structure by atomic layer deposition. The gate contact was subsequently produced in the same manner as the other contacts. The

resulting device has a channel length of $L = 1.4\,\mu m$ and a width of $W = 2\,\mu m$, which was limited by the exposure tool. The electrical characterization of the finished devices was performed on a Cascade probe station with a Keithley 4200 SCS system at room temperature and ambient conditions.

Supporting Information

Supporting Information is available from the Wiley Online Library or from the author.

Acknowledgements

F.V.E.H., V.S., H.P., and D.G.S. acknowledge support from the National Science Foundation [Platform for the Accelerated Realization, Analysis, and Discovery of Interface Materials (PARADIM)] under Cooperative Agreement No. DMR-2039380. P.V., J.K., H.Y., K.S., D.J., H.G.X., S.D, and D.G.S. acknowledge the support from SUPREME and PRISM, two of seven centers in JUMP 2.0, a Semiconductor Research Corporation (SRC) program sponsored by DARPA. K.A. acknowledges the support from the AFOSR/AFRL ACCESS Center of Excellence under Award No. FA9550-18-1-0529. Substrate preparation was performed in part at the Cornell NanoScale Facility, a member of the National Nanotechnology Coordinated Infrastructure (NNCI), which is supported by the National Science Foundation (Grant No. NNCI-2025233). S.L.S. and Z.K.L. acknowledge support from the Endowed Dorothy Pate Enright Professorship at the Pennsylvania State University. This work made use of the Cornell Center for Materials Research Shared Facilities, which are supported through the NSF MRSEC program (DMR-1719875). F.V.E.H. acknowledges funding by the Alexander von Humboldt foundation in the form of a Feodor Lynen fellowship. The authors acknowledge Sean Palmer for substrate preparation and technical support. The authors thank Lena N. Majer for technical support and Marion Kelsch for TEM specimen preperation.

Conflict of Interest

The authors declare no conflict of interest.

Data Availability Statement

The data that support the findings of this study are openly available in the PARADIM data repository at [https://doi.org/10.34863/qrvq-h172].

Keywords

back-end-of-line, field-effect transistor, FET, molecular-beam epitaxy, oxide electronics, transparent electronics, TFT

Received: June 28, 2024
Revised: August 31, 2024
Published online:

[1] G. Thomas, *Nature* **1997**, *389*, 907.
[2] K. Nomura, H. Ohta, K. Ueda, T. Kamiya, M. Hirano, H. Hosono, *Science* **2003**, *300*, 1269.
[3] W. Chakraborty, H. Ye, B. Grisafe, I. Lightcap, S. Datta, *IEEE Trans. Electron Devices* **2020**, *67*, 5336.
[4] M. Si, J. Andler, X. Lyu, C. Niu, S. Datta, R. Agrawal, P. D. Ye, *ACS Nano* **2020**, *14*, 11542.
[5] M. Si, Y. Hu, Z. Lin, X. Sun, A. Charnas, D. Zheng, X. Lyu, H. Wang, K. Cho, P. D. Ye, *Nano Lett.* **2021**, *21*, 500.
[6] M. Si, Z. Lin, A. Charnas, P. D. Ye, *IEEE Electron Device Lett.* **2021**, *42*, 184.
[7] M. Si, A. Charnas, Z. Lin, P. D. Ye, *IEEE Trans. Electron Devices* **2021**, *68*, 1075.
[8] Z. Zhang, Z. Lin, M. Si, D. Zhang, H. Dou, Z. Chen, A. Charnas, H. Wang, P. D. Ye, *Appl. Phys. Lett.* **2022**, *120*, 1.
[9] Z. Lin, M. Si, V. Askarpour, C. Niu, A. Charnas, Z. Shang, Y. Zhang, Y. Hu, Z. Zhang, P.-Y. Liao, K. Cho, H. Wang, M. Lundstrom, J. Maassen, P. D. Ye, *ACS Nano* **2022**, *16*, 21536.
[10] J. Park, H. Paik, K. Nomoto, K. Lee, B.-E. Park, B. Grisafe, L.-C. Wang, S. Salahuddin, S. Datta, Y. Kim, D. Jena, H. G. Xing, D. G. Schlom, *APL Mater.* **2020**, *8*, 011110.
[11] F. V. E. Hensling, W. Braun, D. Y. Kim, L. N. Majer, S. Smink, B. D. Faeth, J. Mannhart, *APL Mater.* **2024**, *12*, 040902.
[12] M. M. S. Aly, M. Gao, G. Hills, C. shuen Lee, G. Pitner, M. M. Shulaker, T. F. Wu, M. Asheghi, J. Bokor, F. Franchetti, K. E. Goodson, C. Kozyrakis, I. Markov, K. Olukotun, L. Pileggi, E. Pop, J. Rabaey, C. Re, H.-S. P. Wong, S. Mitra, *Computer* **2015**, *48*, 24.
[13] S. Datta, S. Dutta, B. Grisafe, J. Smith, S. Srinivasa, H. Ye, *IEEE Micro.* **2019**, *39*, 8.
[14] P. Vogt, D. G. Schlom, F. V. Hensling, K. Azizie, Z.-K. Liu, B. J. Bocklund, S. Shang, *Suboxide molecular-beam epitaxy and related structures*, Penn State Research Foundation and Cornell University, Ithaca **2022**, p. 11462402.
[15] P. Vogt, F. V. Hensling, K. Azizie, C. S. Chang, D. Turner, J. Park, J. P. McCandless, H. Paik, B. J. Bocklund, G. Hoffman, O. Bierwagen, D. Jena, H. G. Xing, S. Mou, D. A. Muller, S. L. Shang, Z. K. Liu, D. G. Schlom, *APL Mater.* **2021**, *9*, 1.
[16] N. Preissler, O. Bierwagen, A. T. Ramu, J. S. Speck, *Phys. Rev. B - Condens. Matter Mater. Phys.* **2013**, *88*, 1.
[17] O. Bierwagen, *Semicond. Sci. Technol.* **2015**, *30*, 24001.
[18] R. A. Stall, *J. Vac. Sci. Technol. B* **1983**, *1*, 135.
[19] H. Aizaki, T. Tatsumi, The Japan Society of Applied Physics Extended Abstracts of the 17th Conference on Solid State Devices and Materials, , Tokyo, **1985**, pp. 301–304.
[20] Y. Kado, Y. Arita, Extended Abstracts of the 20th (1988) International Conference on Solid State Devices and Materials, Tokyo, **1988**, 181–184.
[21] E. Hellman, E. Hartford, T. Palstra, *Phys. C* **1989**, *162*, 633.
[22] M. Passlack, E. F. Schubert, W. S. Hobson, M. Hong, N. Moriya, S. N. G. Chu, K. Konstadinidis, J. P. Mannaerts, M. L. Schnoes, G. J. Zydzik, *J. Appl. Phys.* **1995**, *77*, 686.
[23] M. Hong, J. Kwo, A. R. Kortan, J. P. Mannaerts, A. M. Sergent, *Science* **1999**, *283*, 1897.
[24] P. Vogt, F. V. Hensling, K. Azizie, J. P. McCandless, J. Park, K. DeLello, D. A. Muller, H. G. Xing, D. Jena, D. G. Schlom, *Phys. Rev. Appl.* **2022**, *17*, 034021.
[25] K. Azizie, F. V. E. Hensling, C. A. Gorsak, Y. Kim, N. A. Pieczulewski, D. M. Dryden, M. K. I. Senevirathna, S. Coye, S.-L. Shang, J. Steele, P. Vogt, N. A. Parker, Y. A. Birkhölzer, J. P. McCandless, D. Jena, H. G. Xing, Z.-K. Liu, M. D. Williams, A. J. Green, K. Chabak, D. A. Muller, A. T. Neal, S. Mou, M. O. Thompson, H. P. Nair, D. G. Schlom, *APL Mater.* **2023**, *11*, 041102.
[26] O. Bierwagen, M. E. White, M. Y. Tsai, J. S. Speck, *Appl. Phys. Lett.* **2009**, *95*, 1.
[27] R. A. Cowley, A. Bourlange, J. L. Hutchison, K. H. Zhang, A. M. Korsunsky, R. G. Egdell, *Phys. Rev. B - Condens. Matter Mater. Phys.* **2010**, *82*, 1.
[28] Y. L. Hu, E. Rind, J. S. Speck, *J. Appl. Crystallogr.* **2014**, *47*, 443.
[29] M. R. Karim, Z. Feng, H. Zhao, *Cryst. Growth Des.* **2018**, *18*, 4495.
[30] O. Bierwagen, J. S. Speck, *Appl. Phys. Lett.* **2010**, *97*, 3.
[31] P. Vogt, O. Bierwagen, *Phys. Rev. Mater.* **2018**, *2*, 1.

[32] P. Vogt, O. Bierwagen, *Appl. Phys. Lett.* **2015**, *106*, 1.
[33] P. Vogt, O. Bierwagen, *Appl. Phys. Lett.* **2016**, *109*, 062103.
[34] J. R. Arthur, *J. Appl. Phys.* **1968**, *39*, 4032.
[35] K. G. Guenther, *Die Naturwissenschaften* **1958**, *45*, 415.
[36] H. Freller, K. Günther, *Thin Solid Films* **1982**, *88*, 291.
[37] R. Heckingbottom, G. J. Davies, K. A. Prior, *Surf. Sci.* **1983**, *132*, 375.
[38] H. Seki, A. Koukitu, *J. Cryst. Growth* **1986**, *78*, 342.
[39] J. Tsao, *J. Cryst. Growth* **1991**, *110*, 595.
[40] J. Tsao, *Materials Fundamentals of Molecular Beam Epitaxy*, Academic Press, Washington, DC **1993**.
[41] K. M. Adkison, S.-L. Shang, B. J. Bocklund, D. Klimm, D. G. Schlom, Z.-K. Liu, *APL Mater.* **2020**, *8*, 081110.
[42] S. Ghose, M. S. Rahman, J. S. Rojas-Ramirez, M. Caro, R. Droopad, A. Arias, N. Nedev, *J. Vac. Sci. Technol., B: Nanotechnol. Microelectron.: Mater., Process., Meas., Phenom.* **2016**, *34*, 02L109.
[43] S. Ghose, S. Rahman, L. Hong, J. S. Rojas-Ramirez, H. Jin, K. Park, R. Klie, R. Droopad, *J. Appl. Phys.* **2017**, *122*, 095302.
[44] M. Passlack, J. Abrokwah, R. Droopad, C. Overgaard, Iii-v epitaxial wafer production, US006030453A, **2000**.
[45] M. Passlack, J. Abrokwah, Z. Yu, Ultraviolet transmitting oxide with metallix oxide phase and method of fabrication, US006094295A, **2000**.
[46] M. Passlack, Z. Yu, R. Droopad, J. Abrokwah, D. Braddock, S.-I. Yi, M. Hale, J. Sexton, A. Kummel, *Gallium Oxide on Gallium Arsenide: Atomic Structure, Materials, and Devices III-V Semiconductor Heterostructures: Physics and Devices*, Research Signpost, Kerala **2003**, pp. 1–29.
[47] G. Hoffmann, M. Budde, P. Mazzolini, O. Bierwagen, *APL Mater.* **2020**, *8*, 031110.
[48] L. für Theoretische Hüttenkunde, ed., *Scientific Group Thermodata Europe (SGTE) Landolt-Börnstein: Numerical Data and Functional Relationships in Science and Technology, New Series, Group IV; Lehrstuhl für Theoretische Hüttenkunde*, 19a edn., Springer Verlag, Berlin/Heidelberg **1999**.
[49] J. O. Andersson, T. Helander, L. Höglund, P. Shi, B. Sundman, *CALPHAD: Comput. Coupling Phase Diagrams Thermochem.* **2002**, *26*, 273.
[50] E. H. Smith, P. D. C. King, A. Soukiassian, D. G. Ast, D. G. Schlom, *Appl. Phys. Lett.* **2017**, *111*, 131903.
[51] S. J. Skinner, J. A. Kilner, *Mater. Today* **2003**, *6*, 30.
[52] N. Miyata, *Sci. Rep.* **2018**, *8*, 1.
[53] C. Park, U. Kim, C. J. Ju, J. S. Park, Y. M. Kim, K. Char, *Appl. Phys. Lett.* **2014**, *105*, 1.
[54] U. Kim, C. Park, T. Ha, Y. M. Kim, N. Kim, C. Ju, J. Park, J. Yu, J. H. Kim, K. Char, *APL Mater.* **2015**, *3*, 036101.
[55] J. Shin, Y. M. Kim, Y. Kim, C. Park, K. Char, *Appl. Phys. Lett.* **2016**, *109*, 262102.
[56] Y. M. Kim, C. Park, T. Ha, U. Kim, N. Kim, J. Shin, Y. Kim, J. Yu, J. H. Kim, K. Char, *APL Mater.* **2017**, *5*, 016104.
[57] Y. Kim, Y. M. Kim, J. Shin, K. Char, *APL Mater.* **2018**, *6*, 096104.
[58] J. Cheng, H. Yang, C. Wang, N. Combs, C. Freeze, O. Shoron, W. Wu, N. K. Kalarickal, H. Chandrasekar, S. Stemmer, S. Rajan, W. Lu, *J. Vac. Sci. Technol., B: Nanotechnol. Microelectron.: Mater., Process., Meas., Phenom.* **2020**, *38*, 012201.
[59] J. Park, H. Paik, K. Nomoto, K. Lee, B. E. Park, B. Grisafe, L. C. Wang, S. Salahuddin, S. Datta, Y. Kim, D. Jena, H. G. Xing, D. G. Schlom, *APL Mater.* **2020**, *8*, 011110.
[60] J. Cheng, C. Wang, C. Freeze, O. Shoron, N. Combs, H. Yang, N. K. Kalarickal, Z. Xia, S. Stemmer, S. Rajan, W. Lu, *IEEE Electron Device Lett.* **2020**, *41*, 621.
[61] Y. M. Kim, C. Park, U. Kim, C. Ju, K. Char, *Appl. Phys. Express* **2016**, *9*, 011201.
[62] W. S. Hwang, A. Verma, H. Peelaers, V. Protasenko, S. Rouvimov, H. Xing, A. Seabaugh, W. Haensch, C. V. D. Walle, Z. Galazka, M. Albrecht, R. Fornari, D. Jena, *Appl. Phys. Lett.* **2014**, *104*, 3.
[63] N. A. Moser, J. P. McCandless, A. Crespo, K. D. Leedy, A. J. Green, E. R. Heller, K. D. Chabak, N. Peixoto, G. H. Jessen, *Appl. Phys. Lett.* **2017**, *110*, 143505.
[64] H. Zhou, K. Maize, G. Qiu, A. Shakouri, P. D. Ye, *Appl. Phys. Lett.* **2017**, *111*, 092102.
[65] H. Zhou, K. Maize, J. Noh, A. Shakouri, P. D. Ye, *ACS Omega* **2017**, *2*, 7723.
[66] Z. Xia, C. Joishi, S. Krishnamoorthy, S. Bajaj, Y. Zhang, M. Brenner, S. Lodha, S. Rajan, *IEEE Electron Device Lett.* **2018**, *39*, 568.
[67] M. Higashiwaki, K. Sasaki, T. Kamimura, M. H. Wong, D. Krishnamurthy, *Japanese J. Appl. Phys.* **2013**, *3*, 3.
[68] K. D. Chabak, J. P. McCandless, N. A. Moser, A. J. Green, K. Mahalingam, A. Crespo, N. Hendricks, B. M. Howe, S. E. Tetlak, K. Leedy, R. C. Fitch, D. Wakimoto, K. Sasaki, A. Kuramata, G. H. Jessen, *IEEE Electron Device Lett.* **2018**, *39*, 67.
[69] A. J. Green, K. D. Chabak, M. Baldini, N. Moser, R. Gilbert, R. C. Fitch, G. Wagner, Z. Galazka, J. Mccandless, A. Crespo, K. Leedy, G. H. Jessen, *IEEE Electron Device Lett.* **2017**, *38*, 790.
[70] R. Yao, Z. Zheng, M. Xiong, X. Zhang, X. Li, H. Ning, Z. Fang, W. Xie, X. Lu, J. Peng, *Appl. Phys. Lett.* **2018**, *112*, 1.
[71] K. Nomura, H. Ohta, K. Ueda, T. Kamiya, M. Hirano, H. Hosono, *Science* **2003**, *300*, 1269.
[72] N. C. Su, S. J. Wang, A. Chin, *IEEE Electron Device Lett.* **2009**, *30*, 1317.
[73] K. Nomura, H. Ohta, A. Takagi, T. Kamiya, M. Hirano, H. Hosono, *Nature* **2004**, *432*, 488.
[74] Z. Yuan, X. Zhu, X. Wang, X. Cai, B. Zhang, D. Qiu, H. Wu, *Thin Solid Films* **2011**, *519*, 3254.
[75] P. K. Nayak, M. N. Hedhili, D. Cha, H. N. Alshareef, *Appl. Phys. Lett.* **2013**, *103*, 1.
[76] N. Mitoma, S. Aikawa, X. Gao, T. Kizu, M. Shimizu, M. F. Lin, T. Nabatame, K. Tsukagoshi, *Appl. Phys. Lett.* **2014**, *104*, 102103.
[77] L. Wang, M. H. Yoon, G. Lu, Y. Yang, A. Facchetti, T. J. Marks, *Nat. Mater.* **2006**, *5*, 893.
[78] M. Si, J. Andler, X. Lyu, C. Niu, S. Datta, R. Agrawal, P. D. Ye, *ACS Nano* **2020**, *14*, 11542.
[79] S. Li, M. Tian, Q. Gao, M. Wang, T. Li, Q. Hu, X. Li, Y. Wu, *Nat. Mater.* **2019**, *18*, 1091.
[80] I. Noviyana, A. D. Lestari, M. Putri, M. S. Won, J. S. Bae, Y. W. Heo, H. Y. Lee, *Materials* **2017**, *10*, 1.
[81] S. Tomai, M. Nishimura, M. Itose, M. Matuura, M. Kasami, S. Matsuzaki, H. Kawashima, F. Utsuno, K. Yano, *Japanese J. Appl. Phys.* **2012**, *51*, 03CB01.
[82] R. Jany, C. Richter, C. Woltmann, G. Pfanzelt, B. Förg, M. Rommel, T. Reindl, U. Waizmann, J. Weis, J. A. Mundy, D. A. Muller, H. Boschker, J. Mannhart, *Adv. Mater. Interfaces* **2014**, *1*, 1.
[83] L. Dong, Y. Liu, M. Xu, Y. Wu, R. Colby, E. Stach, R. Droopad, R. Gordon, P. D. Ye, *Int. Electron Devices Meeting*, IEEE, San Francisco, CA, USA **2010**, p. 26.
[84] C. Ju, C. Park, H. Yang, U. Kim, Y. M. Kim, K. Char, *Curr. Appl. Phys.* **2016**, *16*, 300.
[85] R. E. Presley, C. L. Munsee, C. H. Park, D. Hong, J. F. Wager, D. A. Keszler, *J. Phys. D: Appl. Phys.* **2004**, *37*, 2810.
[86] P. F. Carcia, R. S. McLean, M. H. Reilly, G. Nunes, *Appl. Phys. Lett.* **2003**, *82*, 1117.
[87] H. H. Hsieh, C. C. Wu, *Appl. Phys. Lett.* **2006**, *89*, 041109.
[88] B. Bayraktaroglu, K. Leedy, R. Neidhard, *IEEE Electron Device Lett.* **2009**, *30*, 946.
[89] B. Bayraktaroglu, K. Leedy, R. Neidhard, *IEEE Electron Device Lett.* **2008**, *29*, 1024.

[90] B. Y. Oh, Y. H. Kim, H. J. Lee, B. Y. Kim, H. G. Park, J. W. Han, G. S. Heo, T. W. Kim, K. Y. Kim, D. S. Seo, *Semicond. Sci. Technol.* **2011**, *26*, 085007.
[91] X. Cheng, B. Lu, J. Lu, S. Li, R. Lu, S. Yue, L. Chen, Z. Ye, *IEEE Trans. Electron Devices* **2020**, *67*, 2336.
[92] W. K. Min, S. P. Park, H. J. Kim, J. H. Lee, K. Park, D. Kim, K. W. Kim, H. J. Kim, *ACS Appl. Mater. Interf.* **2020**, *12*, 24929.
[93] X. Zou, G. Fang, L. Yuan, M. Li, W. Guan, X. Zhao, *IEEE Electron Device Lett.* **2010**, *31*, 827.
[94] H. Hu, J. Zhu, M. Chen, T. Guo, F. Li, *Appl. Surf. Sci.* **2018**, *441*, 295.
[95] T. Lin, X. Li, J. Jang, *Appl. Phys. Lett.* **2016**, *108*, 233503.
[96] F. Shan, A. Liu, H. Zhu, W. Kong, J. Liu, B. Shin, E. Fortunato, R. Martins, G. Liu, *J. Mater. Chem. C* **2016**, *4*, 9438.
[97] H. S. Jeong, M. J. Park, S. H. Kwon, H. J. Joo, H. I. Kwon, *Sens. Actuators, B* **2019**, *288*, 625.
[98] S. Yim, T. Kim, B. Yoo, H. Xu, Y. Youn, S. Han, J. K. Jeong, *ACS Appl. Mater. Interf.* **2019**, *11*, 47025.
[99] S. D. Bae, S. H. Kwon, H. S. Jeong, H. I. Kwon, *Semicond. Sci. Technol.* **2017**, *32*, 075006.
[100] Y. Ogo, H. Hiramatsu, K. Nomura, H. Yanagi, T. Kamiya, M. Hirano, H. Hosono, *Appl. Phys. Lett.* **2008**, *93*, 1.
[101] J. A. Caraveo-Frescas, P. K. Nayak, H. A. Al-Jawhari, D. B. Granato, U. Schwingenschlögl, H. N. Alshareef, *ACS Nano* **2013**, *7*, 5160.
[102] C. W. Shih, A. Chin, C. F. Lu, W. F. Su, *Sci. Rep.* **2018**, *8*, 1.
[103] A. Zavabeti, P. Aukarasereenont, H. Tuohey, N. Syed, A. Jannat, A. Elbourne, K. A. Messalea, B. Y. Zhang, B. J. Murdoch, J. G. Partridge, M. Wurdack, D. L. Creedon, J. van Embden, K. Kalantar-Zadeh, S. P. Russo, C. F. McConville, T. Daeneke, *Nat. Electron.* **2021**, *4*, 277.
[104] D. M. Binkley, B. J. Blalock, J. M. Rochelle, *Analog Integr. Circuits Signal Process.* **2006**, *47*, 137.
[105] D. Schlom, J. Harris, *Molecular Beam Epitaxy: Application to Key Materials*, William Andrew, Noyes, Park Ridge **1995**, pp. 505–622.
[106] N. Taga, M. Maekawa, Y. Shuigesato, I. Yasui, M. Kakei, T. E. Haynes, *Jpn J. Appl. Phys., Part 1* **1998**, *37*, 6524.
[107] O. Lozano, Q. Y. Chen, P. V. Wadekar, H. W. Seo, P. V. Chinta, L. H. Chu, L. W. Tu, I. Lo, S. W. Yeh, N. J. Ho, F. C. Chuang, D. J. Jang, D. Wijesundera, W. K. Chu, *Sol. Energy Mater. Sol. Cells* **2013**, *113*, 171.
[108] H. Ohta, M. Orita, M. Hirano, H. Tanji, H. Kawazoe, H. Hosono, *Appl. Phys. Lett.* **2000**, *76*, 2740.
[109] P. D. C. King, T. D. Veal, D. J. Payne, A. Bourlange, R. G. Egdell, C. F. McConville, *Phys. Rev. Lett.* **2008**, *101*, 116808.
[110] Z. Galazka, K. Irmscher, M. Pietsch, T. Schulz, R. Uecker, D. Klimm, R. Fornari, *CrystEngComm* **2013**, *15*, 2220.

